The Effect of an Embedded Solid Block on the Onset of Convection in a Porous Cavity

[1]**D. Andrew S. Rees,** [2]**D. A. Nield**

[1] *Department of Mechanical Engineering, University of Bath, Bath BA2 7AY, UK.*
[2] *Department of Engineering Science, University of Auckland, Private Bag 92019, Auckland 1142, New Zealand.*

✉ D.A.S.Rees@bath.ac.uk d.nield@auckland.ac.nz

Abstract

Purpose – The purpose is to determine how the presence of an embedded, centrally-placed, solid but heat-conducting block affects the onset and development of Darcy-Bénard convection.

Design/methodology/approach – Steady solutions are obtained using finite difference methods with SOR as the smoother. A detailed presentation is given of how the interface conditions are modelled, and how a continuity of pressure argument is used to determine the value of the streamfunction on the solid block.

Findings – The presence of the block affects strongly both the onset of convection and the nonlinear properties such as the mean Nusselt number and the strength of the fluid circulation. The smallest possible critical Darcy-Rayleigh number is found to be 22.0152, which is much smaller than $4\pi^2$, the value when the block is absent.

Research limitations/implications – The Darcy-Rayleigh number is restricted to values at or below 200, which is five times the critical value without a solid block, but the size and conductivity of the block vary between all admissible values.

Originality/value – This is the first investigation of the effect of internal obstacles on Darcy-Bénard convection.

Keywords – Porous media, convection, onset, nonlinear flow, square cavity, embedded solid block.

Paper type – Research paper.

Nomenclature

C	heat capacity
$\mathscr{C}$	circulation strength ($\|\psi\|_{\max}$)
g	gravity
h	step length
i	index for grid points in the x-direction
i_1, i_2, j_1, j_2	indices defining the edges of the block
j	index for grid points in the z-direction
k	thermal conductivity
K	permeability
L	height and width of the cavity
n	intervals comprising the block
N	intervals comprising the cavity
Nu	Nusselt number
p	pressure
Ra	Darcy-Rayleigh number
t	time
T	dimensional temperature
u	horizontal velocity
w	vertical velocity
x	horizontal coordinate
z	vertical coordinate

Greek symbols

α	diffusivity ratio
β	expansion coefficient
ϵ	block to cavity aspect ratio, (n/N)
θ	temperature
κ	conductivity ratio
μ	dynamic viscosity
ρ	density
ψ	streamfunction

Subscripts, superscripts, and other symbols

c	cold
f	fluid
h	hot
i, j	denoting grid points
pm	porous medium
$\hat{}$	dimensional quantity
$\mathfrak{T}$	trapezium rule summation given in (36)

1 Introduction

Hydrologists are interested in whether a given geothermal gradient or salinity gradient is sufficiently strong to induce a significant amount of convection in fractured rock (see, for example, Simmons et al. (2007)). Of especial interest is the case where the fracturing is sufficiently extensive to produce connected channels linked to form loops in which the fluid can circulate on a relatively large length scale. This is a complicated situation for which analysis is difficult. It is desirable as a preliminary step to understand what happens in a single loop, and then later in a small number of linked loops.

Most of the published studies of convection loops involved heating from the side. Many of these have been concerned with thermo-syphons, and for these the primary topic of interest is heat transfer. Examples are the studies by Greif and colleagues, such as Greif et al. (1979), Lavine et al. (1986, 1987), Mertol et al. (1982), Stern and Greif (1987) and Stern et al. (1988). The earlier work was reviewed by Mertol and Greif (1985). Another reason for the interest in heating from the side is that oscillatory motion and then transition to chaotic flow occur as the Rayleigh number is increased (see, for example, Gorman et al. (1984), Ehrhard and Mueller (1990). This situation can be modelled by a Lorenz system of equations. Feedback control of the chaos is a topic of recent research (see, for example, Ridouane et al. (2010, 2011)). In the studies cited above a circular loop was involved. A square loop was examined by Acosta et al. (1987) and Ramos et al. (1990). So far the publications cited have involved a fluid clear of solid material. A loop filled with a porous medium has been studied by Robillard et al. (1986), Paterson and Schlanger (1992), Magomedbekov and Ramazanov (1994, 1996), Ramazanov (2000), Scurtu et al. (2001), Jiang and Shoji (2002) and Postelnicu and Scurtu (2005).

Thus there is an extensive literature on closed convection loops. However, of the above papers only those by Scurtu et al. (2001) and Magomedbekov and Ramazanov (1996) were concerned with the onset of steady convection. (The earlier papers by Keller (1966) and Welander (1967) were concerned with the oscillations

(in velocity, not in direction) that initially appear when the heating is started but which subsequently decay.) Each of these papers involved what is essentially a two-dimensional flow, in the space between two concentric cylinders. The pioneering papers are those by Sano (1986, 1991), who did investigate a vertical temperature gradient. Scurtu et al. (2001) repeated the analysis of Sano (1986) for a porous medium instead of a clear fluid. The work of Magomedbekov and Ramazanov (1996) is independent of that of the other authors and is mainly concerned with the appearance of higher-order modes.

We note that a vertical annular loop is a special case of a horizontal annulus, one in which the dimension in the axial direction is very small. Hence we note the existence of previous publications on convection in horizontal annuli in a porous medium surveyed in Sections 6.16.2 of Nield and Bejan (2013). In a geophysical situation the boundaries will be approximately planar, and so it will be rectangular loops rather than circular loops that will be of interest. However, the geometry is now more complicated and it likely that no simple analytical relationships exist, and consequently numerical studies are needed. In the absence of anything more accurate, Nield (2015) proposed a method of estimating the critical Rayleigh number for a rectangular loop in rock of small permeability and small thermal conductivity. He considered the case of an annulus between two concentric square cylinders each with vertical and horizontal boundaries — this is a variant on the well-known Darcy-Bénard or Horton-Rogers-Lapwood problem. He regarded the problem as one involving an extremely heterogeneous porous medium whose domain is the interior of the outer square, with a subdomain formed by the inner square in which the permeability K and the thermal conductivity k are each zero. He concluded that the critical Rayleigh number for the annulus could be given a ballpark estimate by supposing that the inner cylinder is absent. He emphasized that this holds only when the rock has small permeability and small thermal conductivity. In other cases the inner cylinder has the effect of leaking buoyancy force out of the loop (via a reduction in temperature contrast and thus a reduction in density contrast), and hence the effect would be stabilizing. The discussion by Nield (2015) is obviously speculative. Hence we are now testing his ideas by performing accurate computations.

We envisage this paper as a first step in a possibly extensive investigation. Convection in both a porous medium and a fluid without a solid matrix are of interest, but we confine our attention to the former. Examples of the latter include papers such as those of House et al. (1990), Bhave et al. (2006), Rahman et al. (2009), Hooman et al. (2010), Bararnia et al. (2011) and Roslan et al. (2014), but while these works examine different types of obstacle within the cavity, they are devoted to differential heating across the cavity rather than heating from below. We perform computations on a domain with very simple geometry, namely a two-dimensional square enclosure aligned vertically in which is placed a similarly aligned solid block positioned centrally (Figure 1). We confine our attention to steady flow which will give rise to three governing nondimensional parameters. It is, of course, possible to include further 'effects', such as form drag (one parameter), Brinkman terms (one parameter), anisotropy (up to four parameters), Local Thermal Non-Equilibrium (two parameters) and a non-centrally located block (two parameters), but we have imposed a three-parameter limit in order to be able to provide a fully comprehensive account of the central issue, namely how a conducting solid block might alter the well-known Darcy-Bénard problem.

The computation has two unusual features that present potential difficulties, namely (i) the need to model the interface between the porous medium and the solid block, and (ii) the need to determine the value of a streamline on the block itself. We tackle these difficulties using an idea drawn from the network modelling analysis of Jamaludin-Din et al. (2010) and recently used by Rees (2015) in the context of the convection of Bingham fluids in porous media.

2 Governing Equations

We consider convection in a square porous cavity which is heated from below and within which is embedded centrally a conducting solid square block; see Fig. 1. The height of the cavity is L and that of the block is ϵL, and therefore ϵ represents the ratio of the sides of the respective squares. The upper and lower horizontal surfaces are assumed to be subject to uniform fixed temperatures, $T = T_c$ and $T = T_h$, respectively, and the sidewalls are insulated. On the other hand, the surfaces of the block are impermeable, but it is necessary for them to satisfy the continuity of both temperature and heat flux.

The conservation of mass corresponds to

$$\frac{\partial \hat{u}}{\partial \hat{x}} + \frac{\partial \hat{w}}{\partial \hat{z}} = 0, \tag{1}$$

while Darcy's law for a Newtonian fluid which is subject to the Boussinesq approximation takes the form

$$\hat{u} = -\frac{K}{\mu}\frac{\partial \hat{p}}{\partial \hat{x}}, \tag{2}$$

$$\hat{w} = -\frac{K}{\mu}\left[\frac{\partial \hat{p}}{\partial \hat{z}} - \rho_{\rm f} g\beta(T - T_c)\right]. \tag{3}$$

The heat transport equation for the porous region is given by

$$(\rho C)_{\rm pm}\frac{\partial T_{\rm pm}}{\partial \hat{t}} + (\rho C)_{\rm f}\Big[\hat{u}\frac{\partial T_{\rm pm}}{\partial \hat{x}} + \hat{w}\frac{\partial T_{\rm pm}}{\partial \hat{z}}\Big] = k_{\rm pm}\Big[\frac{\partial^2 T_{\rm pm}}{\partial \hat{x}^2} + \frac{\partial^2 T_{\rm pm}}{\partial \hat{z}^2}\Big], \tag{4}$$

while that for the solid block is

$$(\rho C)_{\rm s}\frac{\partial T_{\rm s}}{\partial \hat{t}} = k_{\rm s}\Big[\frac{\partial^2 T_{\rm s}}{\partial \hat{x}^2} + \frac{\partial^2 T_{\rm s}}{\partial \hat{z}^2}\Big]. \tag{5}$$

The detailed boundary conditions may be seen in Figure 1, but the following continuity conditions need to be applied at the interface between the porous medium and the solid block

$$T_{\rm pm} = T_{\rm s}, \qquad k_{\rm pm}\frac{\partial T_{\rm pm}}{\partial n} = k_{\rm s}\frac{\partial T_{\rm s}}{\partial n}, \tag{6}$$

where n denotes the direction which is normal to the interface.

These equations and boundary/interface conditions may be made dimensionless by using the following scalings

$$\hat{t} = \frac{L^2(\rho C)_{\rm pm}}{k_{\rm pm}}, \qquad (\hat{x}, \hat{z}) = L(x, z), \qquad (\hat{u}, \hat{w}) = \frac{k_{\rm pm}}{L(\rho C)_{\rm f}}(u, w), \qquad T = T_c + \theta(T_h - T_c). \tag{7}$$

Equations (1)–(4) become

$$\frac{\partial u}{\partial x} + \frac{\partial w}{\partial z} = 0, \tag{8}$$

$$u = -\frac{\partial p}{\partial x}, \tag{9}$$

$$w = -\frac{\partial p}{\partial z} + {\rm Ra}\,\theta_{\rm pm}, \tag{10}$$

and

$$\frac{\partial \theta_{\rm pm}}{\partial t} + u\frac{\partial \theta_{\rm pm}}{\partial x} + w\frac{\partial \theta_{\rm pm}}{\partial z} = \frac{\partial^2 \theta_{\rm pm}}{\partial x^2} + \frac{\partial^2 \theta_{\rm pm}}{\partial z^2}. \tag{11}$$

As we will be considering solely two-dimensional convection we may define the streamfunction, ψ, using

$$u = -\frac{\partial \psi}{\partial z}, \qquad w = \frac{\partial \psi}{\partial x}, \tag{12}$$

which means that Eq. (8) is satisfied automatically. Thus the elimination of p between Eqs. (9) and (10) means that the nondimensional governing equations for the porous medium and the boundary conditions become

$$\frac{\partial^2 \psi}{\partial x^2} + \frac{\partial^2 \psi}{\partial z^2} = {\rm Ra}\frac{\partial \theta_{\rm pm}}{\partial x}, \tag{13}$$

$$\frac{\partial \theta_{\rm pm}}{\partial t} + \frac{\partial \psi}{\partial x}\frac{\partial \theta_{\rm pm}}{\partial z} - \frac{\partial \psi}{\partial z}\frac{\partial \theta_{\rm pm}}{\partial x} = \frac{\partial^2 \theta_{\rm pm}}{\partial x^2} + \frac{\partial^2 \theta_{\rm pm}}{\partial z^2}, \tag{14}$$

$$\begin{aligned} x = 0,\ x = 1: \qquad & \psi = 0, \quad \frac{\partial \theta_{\rm pm}}{\partial x} = 0, \\ z = 0,\ z = 1: \qquad & \psi = 0, \quad \theta_{\rm pm} = 1 - z. \end{aligned} \tag{15}$$

The corresponding heat transport equation and interface conditions for solid block are

$$\frac{\partial \theta_{\rm s}}{\partial t} = \alpha\Big[\frac{\partial^2 \theta_{\rm s}}{\partial x^2} + \frac{\partial^2 \theta_{\rm s}}{\partial z^2}\Big], \tag{16}$$

$$\theta_{\rm pm} = \theta_{\rm s}, \qquad \frac{\partial \theta_{\rm pm}}{\partial n} = \kappa \frac{\partial \theta_{\rm s}}{\partial n}. \tag{17}$$

The values, α and κ, are the diffusivity and conductivity ratios, and they are given by

$$\alpha = \frac{k_{\rm s}(\rho C)_{\rm f}}{k_{\rm pm}(\rho C)_{\rm s}}, \qquad \kappa = \frac{k_{\rm s}}{k_{\rm pm}}, \tag{18}$$

where the Darcy-Rayleigh number is given by

$$\mathrm{Ra} = \frac{\rho_{\rm f} g \beta (T_h - T_c) K L}{\mu (k_{pm}/(\rho C)_{\rm f})}. \tag{19}$$

Steady convection is now seen to be governed by three dimensionless parameters, ϵ, κ and Ra. For unsteady convection the diffusivity ratio, α, is the fourth parameter.

3 Numerical method

Equations (13) to (17) are solved using standard finite difference methods which are based upon second-order accurate central difference approximations. The difference equations corresponding to steady-state solutions are solved using Successive over-Relaxation. However, the present problem features two difficulties which are not often present in nonlinear computations, namely (i) that of modelling the interface condition between the porous medium and the solid block, and (ii) that of determining the value of the streamfunction on the block itself. Therefore this section will concentrate in some detail on how these difficulties were addressed.

Internal points. First, we have taken equal steplengths, h, in the x and z-directions, and therefore the grid points will be labelled between 0 and N where $Nh = 1$. We may label the grid points as $x_i = ih$ and $z_j = jh$ where $\psi_{i,j}$ and $\theta_{i,j}$ are the numerical approximations to the exact solutions for ψ and θ at $(x, z) = (x_i, z_j)$. Using the finite difference molecule notation, the discretized form of Eq. (13) may be written in the form

$$\frac{1}{h^2}\begin{pmatrix} 0 & 1 & 0 \\ 1 & -4 & 1 \\ 0 & 1 & 0 \end{pmatrix} \psi_{i,j} = \mathrm{Ra}\,\frac{1}{2h}\begin{pmatrix} -1 & 0 & 1 \end{pmatrix} \theta_{i,j}, \tag{20}$$

and this is applied on all the interior points in the porous medium. The corresponding difference equations for the heat transport equations, (14) and (16) are, respectively

$$\frac{\partial \theta_{i,j}}{\partial t} + \frac{1}{4h^2}\left[\begin{pmatrix} -1 & 0 & 1 \end{pmatrix}\psi_{i,j}\begin{pmatrix} 1 \\ 0 \\ -1 \end{pmatrix}\theta_{i,j} - \begin{pmatrix} 1 \\ 0 \\ -1 \end{pmatrix}\psi_{i,j}\begin{pmatrix} -1 & 0 & 1 \end{pmatrix}\theta_{i,j}\right] = \frac{1}{h^2}\begin{pmatrix} 0 & 1 & 0 \\ 1 & -4 & 1 \\ 0 & 1 & 0 \end{pmatrix}\theta_{i,j}, \tag{21}$$

and

$$\frac{\partial \theta_{i,j}}{\partial t} = \frac{\alpha}{h^2} \begin{pmatrix} 0 & 1 & 0 \\ 1 & -4 & 1 \\ 0 & 1 & 0 \end{pmatrix} \theta_{i,j}, \tag{22}$$

where we have not differentiated in terms of notation between those grid points which correspond to the porous medium and those to the solid. In addition, we have not discretised in time because steady solutions simply ignore the time derivatives, but we will retain the time-derivatives as a reference for future studies on unsteady convection.

Side walls. We will need to apply Eq. (21) at at $i = 0$ (i.e. $x = 0$, the left hand boundary) but this introduces the so-called ghost or fictitious points, $\psi_{-1,j}$ and $\theta_{-1,j}$ which lie outside of the computational domain. However, the boundary conditions there are that $\psi = 0$ and $\partial\theta/\partial x = 0$. The latter may be discretised to yield, $\theta_{-1,j} = \theta_{i,j}$, which may be used to eliminate the temperature ghost point in the central difference approximation to Eq. (21). An examination of Eq. (20) at $i = 0$ (which we do not need to apply in order to solve the equations since ψ is known on the boundary) yields, $\psi_{-1,j} = -\psi_{1,j}$. Therefore we are now in a position to apply Eq. (21) and to express it solely in terms of internal and boundary nodes:

$$\frac{\partial \theta_{0,j}}{\partial t} + \frac{1}{4h^2} \begin{pmatrix} 0 & 0 & 2 \end{pmatrix} \psi_{0,j} \begin{pmatrix} 1 \\ 0 \\ -1 \end{pmatrix} \theta_{0,j} = \frac{1}{h^2} \begin{pmatrix} 0 & 1 & 0 \\ 0 & -4 & 2 \\ 0 & 1 & 0 \end{pmatrix} \theta_{0,j}. \tag{23}$$

The corresponding formula at $i = N$, or $x = 1$ is

$$\frac{\partial \theta_{N,j}}{\partial t} + \frac{1}{4h^2} \begin{pmatrix} -2 & 0 & 0 \end{pmatrix} \psi_{N,j} \begin{pmatrix} 1 \\ 0 \\ -1 \end{pmatrix} \theta_{N,j} = \frac{1}{h^2} \begin{pmatrix} 0 & 1 & 0 \\ 2 & -4 & 0 \\ 0 & 1 & 0 \end{pmatrix} \theta_{N,j}. \tag{24}$$

Interfaces. We will concentrate on the left hand interface between the porous medium and the solid block, and let $i = I$ there for the purpose of this analysis and for clarity. The values of j will, for now, correspond to points which are not at the two corners. We may extend the idea of the fictitious point technique to this situation by applying both Eq. (21) and Eq. (22) at $i = I$. This yields

$$\frac{\partial \theta_{I,j}}{\partial t} + \frac{1}{4h^2} \begin{pmatrix} -1 & 0 & 1 \end{pmatrix} \psi_{I,j} \begin{pmatrix} 1 \\ 0 \\ -1 \end{pmatrix} \theta_{I,j} = \frac{1}{h^2} \begin{pmatrix} 0 & 1 & 0 \\ 1 & -4 & \boxed{1} \\ 0 & 1 & 0 \end{pmatrix} \theta_{I,j}, \tag{25}$$

where one of the nonlinear terms has disappeared because $\partial\psi/\partial z = 0$ on the boundary of the block, and

$$\frac{\partial \theta_{I,j}}{\partial t} = \frac{\alpha}{h^2} \begin{pmatrix} 0 & 1 & 0 \\ \boxed{1} & -4 & 1 \\ 0 & 1 & 0 \end{pmatrix} \theta_{I,j}. \tag{26}$$

The two coefficients which are boxed are the two fictitious points. The one in Eq. (25) is a porous medium term stationed one interval inside the solid region, while the one in Eq. (26) is a solid term one interval inside the porous medium. We may also discretize the continuity-of-heat-flux interface condition, Eq. (17), and this gives

$$\begin{pmatrix} -1 & 0 & \boxed{1} \end{pmatrix} \theta_{I,j} = \kappa \begin{pmatrix} \boxed{\text{-1}} & 0 & 1 \end{pmatrix} \theta_{I,j}. \tag{27}$$

This latest equation may now be used to eliminate the fictitious points. If we multiply both sides of Eq. (26) by κ/α, add the corresponding sides to those of Eq. (25), and use Eq. (27), then we obtain

$$\left(1 + \frac{\kappa}{\alpha}\right) \frac{\partial \theta_{I,j}}{\partial t} + \frac{1}{4h^2} \begin{pmatrix} 0.5 & -2 & 1.5 & 0 & 0 \end{pmatrix} \psi_{I,j} \begin{pmatrix} 1 \\ 0 \\ -1 \end{pmatrix} \theta_{I,j} = \frac{1}{h^2} \begin{pmatrix} 0 & 1+\kappa & 0 \\ 2 & -4(1+\kappa) & 2\kappa \\ 0 & 1+\kappa & 0 \end{pmatrix} \theta_{I,j}, \tag{28}$$

where we note that the central difference approximation to $\partial\psi/\partial x$ which we used earlier has been changed to a second order accurate one-sided difference using grid points which are within the porous medium. The equivalent representation of the heat transport equation at the bottom right corner of the interface is

$$\Big(1+\frac{\kappa}{\alpha}\Big)\frac{\partial\theta_{I,j}}{\partial t}+\frac{1}{4h^2}\begin{pmatrix}0 & 0 & -1.5 & 2 & -0.5\end{pmatrix}\psi_{I,j}\begin{pmatrix}1\\0\\-1\end{pmatrix}\theta_{I,j}=\frac{1}{h^2}\begin{pmatrix}0 & 1+\kappa & 0\\ 2\kappa & -4(1+\kappa) & 2\\ 0 & 1+\kappa & 0\end{pmatrix}\theta_{I,j}, \tag{29}$$

where I now corresponds the the x-index of the right hand interface.

For the lower interface we have

$$\Big(1+\frac{\kappa}{\alpha}\Big)\frac{\partial\theta_{i,J}}{\partial t}-\frac{1}{4h^2}\begin{pmatrix}0\\0\\1.5\\-2\\0.5\end{pmatrix}\psi_{i,J}\begin{pmatrix}-1 & 0 & 1\end{pmatrix}\theta_{i,J}=\frac{1}{h^2}\begin{pmatrix}0 & 2\kappa & 0\\ 1+\kappa & -4(1+\kappa) & 1+\kappa\\ 0 & 2 & 0\end{pmatrix}\theta_{I,j}, \tag{30}$$

where J is the y-index for this interface, and for the upper interface

$$\Big(1+\frac{\kappa}{\alpha}\Big)\frac{\partial\theta_{i,J}}{\partial t}-\frac{1}{4h^2}\begin{pmatrix}-0.5\\2\\-1.5\\0\\0\end{pmatrix}\psi_{i,J}\begin{pmatrix}-1 & 0 & 1\end{pmatrix}\theta_{i,J}=\frac{1}{h^2}\begin{pmatrix}0 & 2 & 0\\ 1+\kappa & -4(1+\kappa) & 1+\kappa\\ 0 & 2\kappa & 0\end{pmatrix}\theta_{I,j}, \tag{31}$$

where J represents this interface.

Interface corners. The determination of the appropriate finite difference approximation for the corners of the solid block is more complicated than for the rest of the interface. To do this we borrow an idea from Rees (2010) in which a conduction problem was solved where each pixel (i.e. the square formed by one interval in each direction) was allowed to have different conductivities. Thus the finite difference approximation was written four times for a given grid point, each approximation representing the 'point of view' of each of the four neighbouring pixels. This produces four fictitious points which may be eliminated by appealing to the four conservation of heat flux conditions which apply between the pixels. In this regard the procedure is identical to that used for the general interface except that two fictitious points were eliminated there. In the present problem, three of the four pixels have identical properties, but the appropriate finite difference approximation may be written by assuming the four conductivities are different, then adding the correct weighted sum of the finite difference approximations, and finally setting the conductivities to the values we require here. We shall omit the detailed derivation of this process.

For the bottom left corner we obtain

$$\begin{aligned}\Big(3+\frac{\kappa}{\alpha}\Big)\frac{\partial\theta_{I,J}}{\partial t}+ \quad 2\times\frac{1}{4h^2}&\left[\begin{pmatrix}0.5 & -2 & 1.5 & 0 & 0\end{pmatrix}\psi_{I,j}\begin{pmatrix}1\\0\\-1\end{pmatrix}\theta_{I,j}-\begin{pmatrix}0\\0\\1.5\\-2\\0.5\end{pmatrix}\psi_{I,J}\begin{pmatrix}-1 & 0 & 1\end{pmatrix}\theta_{I,J}\right]\\ &=\frac{1}{h^2}\begin{pmatrix}0 & 2+2\kappa & 0\\ 4 & -4(3+\kappa) & 2+2\kappa\\ 0 & 4 & 0\end{pmatrix}\theta_{I,J},\end{aligned} \tag{32}$$

where $i=I$ and $=J$ are the indices for this corner. Similar expressions may be written easily for the other three corners, but these are omitted for the sake of brevity. Again, second order accurate one-sided approximations for the derivatives of ψ have been used.

The value of the streamfunction on the block. The interface between the porous medium and the block must correspond to a streamline and therefore each point on the interface must be assigned exactly the same value of the streamfunction. We will denote by ψ_b the value of the streamfunction on the block.

This value may be determined using an idea drawn from a network modelling analysis found in Jamalud-Din et al. (2010) and used more recently in the context of the convection of Bingham fluids in porous media by Rees (2015). The method is derived by insisting that the total change in pressure between the bottom left of the block and the top right is independent of which path around the interface is taken, i.e. along the bottom and up the right side, or up the left side and along the top. If the block lies in the ranges, $x_1 \le x \le x_2$ and $z_1 \le z \le z_2$, then we have

$$\int_{x_1}^{x_2} \frac{\partial p}{\partial x}\Big|_{z=z_1} dx + \int_{z_1}^{z_2} \frac{\partial p}{\partial z}\Big|_{x=x_2} dz = \int_{z_1}^{z_2} \frac{\partial p}{\partial z}\Big|_{x=x_1} dz + \int_{x_1}^{x_2} \frac{\partial p}{\partial x}\Big|_{z=z_2} dx. \tag{33}$$

If we use Eqs. (9) and (10) to write the pressure gradients in terms of the streamfunction and temperature, then this relation takes the form

$$\int_{x_1}^{x_2} \frac{\partial \psi}{\partial z}\Big|_{z=z_1} dx + \int_{z_1}^{z_2} \Big[\mathrm{Ra}\,\theta - \frac{\partial \psi}{\partial x}\Big]_{x=x_2} dz = \int_{z_1}^{z_2} \Big[\mathrm{Ra}\,\theta - \frac{\partial \psi}{\partial x}\Big]_{x=x_1} dz + \int_{x_1}^{x_2} \frac{\partial \psi}{\partial z}\Big|_{z=z_2} dx. \tag{34}$$

Given that we will know the value of θ on all grid points prior to solving for ψ, we may rearrange the above into the form

$$\int_{x_1}^{x_2} \Big(\frac{\partial \psi}{\partial z}\Big|_{z=z_1} - \frac{\partial \psi}{\partial z}\Big|_{z=z_2} \Big) dx + \int_{z_1}^{z_2} \Big(\frac{\partial \psi}{\partial x}\Big|_{x=x_1} - \frac{\partial \psi}{\partial x}\Big|_{x=x_2} \Big) dz = \mathrm{Ra} \int_{z_1}^{z_2} \Big[\theta(x_1,z) - \theta(x_2,z)\Big]\, dz. \tag{35}$$

Both the integrals and the derivatives in Eq. (35) are evaluated numerically, the former using the trapezium rule, while the latter uses one-sided differences from the interface into the porous medium. Presentation of the numerical approximation to (35) is simplified by using the notation

$$\sum_{i=i_1}^{i_2}{}^{\!\!*}\, f_i = \tfrac{1}{2} f_{i_1} + f_{i_1+1} + f_{i_1+2} + \cdots + f_{i_2-1} + f_{i_2-1} + \tfrac{1}{2} f_{i_2}, \tag{36}$$

to represent the summation required to perform the trapezium rule for integration. Therefore, if the grid point i corresponds to $x = x_i$, then

$$\int_{x_1}^{x_2} \theta(x,y)\Big|_{y=y_j} dx \simeq h \sum_{i=i_1}^{i_2}{}^{\!\!*}\, \theta_{i,j}. \tag{37}$$

Here, i_1 and i_2 are the indices which correspond to x_1 and x_2, respectively, and j_1 and j_2 to z_1 and z_2, respectively. If the derivatives of ψ in Eq. (35) are approximated using first order differences using two points within and on the edge of the porous medium, then the value of ψ_b is given by

$$2(i_2 - i_1 + j_2 - j_1)\psi_b = \mathrm{Ra}\, h \sum_{j=j_1}^{j_2}{}^{\!\!*} \Big[\theta_{i_1,j} - \theta_{i_2,j}\Big] + \sum_{i=i_1}^{i_2}{}^{\!\!*} \Big[\psi_{i,j_1-1} + \psi_{i,j_2+1}\Big] + \sum_{j=j_1}^{j_2}{}^{\!\!*} \Big[\psi_{i_1-1,j} + \psi_{i_2+1,j}\Big]. \tag{38}$$

On the other hand, if these derivatives are approximated using one-sided second order differences using three points within and on the edge of the porous medium, then ψ_b is given by

$$\begin{aligned} 3(i_2 - i_1 + j_2 - j_1)\psi_b = \mathrm{Ra}\, h \sum_{j=j_1}^{j_2}{}^{\!\!*} \Big[\theta_{i_1,j} - \theta_{i_2,j}\Big] \quad &+ \sum_{i=i_1}^{i_2}{}^{\!\!*} \Big[-\tfrac{1}{2}\psi_{i,j_1-2} + 2\psi_{i,j_1-1} + 2\psi_{i,j_2+1} - \tfrac{1}{2}\psi_{i,j_2+2}\Big] \\ &+ \sum_{j=j_1}^{j_2}{}^{\!\!*} \Big[-\tfrac{1}{2}\psi_{i_1-2,j} + 2\psi_{i_1-1,j} + 2\psi_{i_2+1,j} - \tfrac{1}{2}\psi_{i+2+2,j}\Big]. \end{aligned} \tag{39}$$

In all our computations we used the latter formula.

Iterations. We solve the steady-state equations using the SOR scheme. Faster schemes such as multigrid are considerably more complicated to program given the presence of the central block than are the case in standard porous cavity. The relaxation parameter was usually set at 1.6, although for lower values of Ra and for finer grids it could take larger values. Convergence was deemed to have taken place when the maximum pointwise change in the temperature field was less than 10^{-8} between iterations. This usually meant that the maximum value of $|\psi|$ and Nu had settled down to at least five significant figures.

Accuracy. If Eq. (39) is selected to find ψ_b, then it means all derivatives and integrations have been approximated using second order accurate formulae. It is to be noted, however, that despite our above efforts to maintain second order accuracy in space, the presence of the re-entrant corners on the block means that perfect second order accuracy cannot be maintained globally. If one considers the homogeneous version of Eq. (13) for ψ, then it is possible to show that eigensolutions exist which are valid near the corners of the block and which satisfy zero values on the surface of the block. These take the form, $\psi \propto r^{2m/3} \sin 2m\vartheta/3$ given that the surfaces of the block subtend an angle of $3\pi/2$, and where m takes positive integer values. Here r is the radial coordinate from a corner and the angular coordinate, ϑ, takes the values 0 and $3\pi/2$. Whilst these eigensolutions remain finite as the corner is approached, the radial derivative is singular in this limit when $m = 1$. It is this singular derivative which provides an unavoidable degradation of the accuracy. The other eigensolutions do not have this property. We have therefore needed to made a careful assessment of the absolute accuracy of the present computations.

It is well-known that accuracy on any chosen fixed grid degrades as parameters such as the Darcy-Rayleigh number increase, but here we are concerned mainly with the numerical effect of the four re-etrant corners. An example of our numerical testing is given in Table 1 which compares the maximum value of $|\psi|$, which is a measure of the total circulation of fluid around the cavity which we denote by $\mathscr{C}$, and the Nusselt number, Nu; these are given by

$$\mathscr{C} = |\psi|_{\max}, \qquad \mathrm{Nu} = -\int_0^1 \frac{\partial \theta}{\partial z}\Big|_{z=1} dx. \tag{40}$$

The integral was evaluated using the trapezium rule and a one-sided difference was used for approximating the derivative. This gives

$$\mathrm{Nu} \simeq \sum_{i=0}^{N} \theta_{i,N-1}. \tag{41}$$

While a two-point one-sided finite difference is usually of first order accuracy, we note that Eq. (14) reduces to $\partial^2\theta/\partial z^2 = 0$ at the surface. Then the use of central differences on this second derivative yields $\theta_{i,N+1} = -\theta_{i,N-1}$, and thus the application of central differences to the derivative in Eq. (40) leads to the same formula as the one-sided difference, thereby rendering the latter of second order accuracy.

Table 1: Values of $\mathscr{C}$ and Nu when Ra = 100 for different values of ϵ and κ. Data is tabulated for both $N = 80$ and 160 in order to assess the accuracy of the computations. Table entries are truncated to five significant figures.

		$\kappa = 1/5$		$\kappa = 1$		$\kappa = 5$	
ϵ	N	$\mathscr{C}$	Nu	$\mathscr{C}$	Nu	$\mathscr{C}$	Nu
0.1	80	5.3952	2.6508	5.3202	2.6476	5.2196	2.6391
	160	5.3867	2.6506	5.3142	2.6477	5.2173	2.6396
0.25	80	5.1732	2.7210	5.0291	2.6766	4.6150	2.5496
	160	5.1544	2.7182	5.0126	2.6740	4.6073	2.5482
0.5	80	4.5978	3.2049	4.0728	2.7870	2.0973	1.8619
	160	4.5738	3.1960	4.0485	2.7767	2.0831	1.8570
0.75	80	2.8762	2.7802	1.7367	1.7909	0.089249	2.2206
	160	2.8621	2.7687	1.7240	1.7828	0.090923	2.2198
0.9	80	0.92171	0.94799	0	1	0.016581	3.3572
	160	0.91957	0.94605	0	1	0.018075	3.3564

Table 1 uses Ra = 100 in all cases, but encompasses a wide range of values of κ. In this Table we see that the relative change in Nu when N changes from 80 to 160 is less than 0.3% in all cases, and is often considerably better than that. Comparison between the values of $\mathscr{C}$ is not quite as good but is still generally much better than 1%. Generally, the best comparisons take place when κ is large and ϵ is small simultaneously, and the worst when κ is small and ϵ is large. Despite this general trend, the poorest comparison in this Table is the case, $\kappa = 5$ and $\epsilon = 0.9$. For such a large value of ϵ the number of grid points comprising the porous channel outside of the block changes from 8 to 16, both values representing very coarse grids, and therefore it is to be expected to see quite a large change. The poor accuracy in this case may be traced to the fact that, while most of the entries in the Table correspond to what will later be called 1-cell flows, this case merely has weak convection near the four narrow corners. The comparison between the values of Nu in this one case are very good indeed, but then heat transfer takes place mostly by conduction. For the case $\epsilon = 0.9$ and $\kappa = 1$, the tabulated values are precise because they reflect the pure conduction state, and convection does not arise.

As a result of these comparisons, we decided to use a grid of 120×120 points for solutions presented in terms of streamlines and isotherms (where $\epsilon = 1/4$ requires N to be divisible by 8), and 100×100 the detailed presentation of the variation in $\mathscr{C}$ and Nu. We also decided to restrict computations in general to values of Ra which are equal to or less than 200; reasons for this are (i) that the number of possible steady-state solutions begins to rise quite markedly at larger values, (ii) persistently unsteady flows can also arise in some parameter regimes, and (iii) it will be necessary to use a finer grid to maintain the levels of accuracy.

4 Results and Discussion

Context. The cavity we are considering corresponds to the classical Darcy-Bénard problem when the block is absent. In genereal, the critical Darcy-Rayleigh number is given by

$$\mathrm{Ra} = \frac{(k^2 + q^2\pi^2)^2}{k^2}, \tag{42}$$

where k is the horizontal wavenumber and q is the number of cells stacked vertically within the cavity/layer. Single-cell convection in a square cavity corresponds to $k = \pi$ and $q = 1$, for which $\mathrm{Ra} = 4\pi^2$. When two cells sit side-by-side then $k = 2\pi$ and $q = 1$ and therefore $\mathrm{Ra} = 6.25\pi^2$. Finally, when there are four cells in

a 2×2 arrangement, then $k = 2\pi$ and $q = 2$, and so $\mathrm{Ra} = 16\pi^2$. All of these values of Ra lie in the range we are considering and have significance in what follows.

Flow patterns. Figure 2 shows the streamline and isotherm fields when $\mathrm{Ra} = 1$. At such a small value of Ra the isotherms are essentially the same as for the purely conducting state, and the streamlines represent a very weak flow. This Figure shows how these fields change depending on the size of the block and the conductivity ratio. When κ is small the isotherms in the porous medium have to enter the block perpendicularly, and this has the overall effect of concentrating the isotherms within the block. The resulting deformation of the isotherms in the porous annulus then induces a set of four counter-rotating cells, where the one in the top left hand corner corresponds to a clockwise circulation. (The direction of circulation is such that the region where the less dense fluid rises is in each case that where the boundary constraint on the flow is less.) This remains true independently of the value of ϵ, but when ϵ is relatively large, these cells are confined solely to the regions near the corners.

When κ increases towards unity, the isotherm deformation decreases and therefore so does the strength of the flow. When $\kappa = 1$ there is only the perfectly conducting state, $\theta = 1 - z$ in both the porous medium and the block, with no flow. At large values of κ the isotherms deform in the opposite direction, thereby causing the upper left hand cell to circulate in the anticlockwise direction. In the most extreme case, $\kappa = 100$, $\epsilon = 3/4$, we see that most of the variation in temperature from the lower to the upper surface of the cavity takes place within the horiizontal porous channels. Thus $\theta \simeq 0.5$ in the block, and therefore the block is hotter in the upper half of the cavity than the sidewalls are, thereby causing a buoyancy-induced flow up the sides of the block.

Figure 3 shows the effect on the streamlines and isotherms of increasing values of Ra for three different values of ϵ when $\kappa = 1$. All the frames depict a Darcy-Bénard convection circulation centred on the block. The strength of the induced convecton may be gauged by the angle taken the isotherms within the block. Noting that weak flow corresponds to horizontal isotherms, one sees, in all cases, that the isotherms rotate clockwise within the block as Ra increases. An increase in the size of the block generally causes the induced flow to decrease in strength, and therefore one sees the isotherms tending back towards the horizontal as ϵ increases. We note that the case, $\mathrm{Ra} = 50$ and $\epsilon = 3/4$ represents conditions which are only just supercritical, and thus the isotherms are almost horizontal.

In the range, $0 \leq \mathrm{Ra} \leq 200$, we find that there are only three main types of flow pattern which exist when a centrally-placed block is present. These are shown in Fig. 4, and are labelled these as 1-cell, 2-cell and 4-cell flows, given the shape of the streamline patterns. As already mentioned, the 1-cell case consists of a convection cell circulating around the block. The 4-cell cases are effectively the basic state the stability of which is being studied. Finally, the 2-cell flow consists of two circulating cells which occupy the sidechannels particularly when ϵ takes larger values. (The two circulating cells occupy vertical sidechannels, rather than the upper and lower horizontal channels, because a wide squat box is more stable than a narrow tall box of the same aspect ratio.) If we concentrate on cases where there is up-flow on the left hand wall of the cavity, then, for $\kappa = 1/10$, we see that the centre of the circulation is above $z = 1/2$. This is because the natural circulation direction caused by the block (see the 4-cell solution) assists the motion of the cell in the upper half of the cavity but inhibits it in the lower half. When $\kappa = 10$, the centre of circulation has moved well below $z = 1/2$ for exactly the same reason. When $\kappa = 1$ the centre is slightly above $z = 1/2$, although the corresponding pattern where there is downflow on the cavity sidewalls will have such a centre slightly below $z = 1/2$.

Solution curves. The primary aim of this paper is to determine the effect of a centrally-placed conducting block on the onset and nonlinear behaviour of convection in a unit porous cavity. Therefore we begin our survey of this effect by showing how $\mathscr{C}$ and Nu vary with ϵ for a range of values of Ra and κ. Figure 5 concentrates on three typical values of Ra, and shows the interplay between the curves for the 1-cell, 2-cell

and 4-cell solutions. These three respective patterns are represented by continuous, dashed and dotted lines.

For all three values of Ra we see that the value of $\mathscr{C}$ for the 1-cell solutions decreases as ϵ increases from zero, which is intuitively what would expect when placing an obstacle in the way of a circulating flow. However, the Nusselt number increases at first, which seems counter-intuitive, before decreasing once more. We may explain this as follows. For the case Ra = 100 and $\kappa = 1/100$, we have $\mathscr{C} = 5.279$ and $\nu = 2.682$ when $\epsilon = 1/5$, and these values change to $\mathscr{C} = 4.333$ to $\nu = 3.573$ when $\epsilon = 3/5$. The channel width (i.e. the perpendicular distance between the block and the cavity wall) has reduced from 2/5 to 1/5 for these two values of ϵ, and therefore the mean velocity along the channels will have increased even though $\mathscr{C}$ has decreased. This brings with it an increased deformation of the isotherms within the porous medium, and in particular a more densely packed set of isotherms at the upper and lower horizontal surfaces. Thus the overall rate of heat transfer increases. This may be seen in Fig. 6. However, as ϵ increases still further (see the $\epsilon = 4/5$ case in Fig. 6), flow tends to become uniform in the narrow channels except near the corners. The upper horizontal channel may then be interpreted as being like the classical Graetz problem with a linear temperature profile at inlet and bounded by two horizontal surfaces, one cold and one insulated. Although the flow is not strong, the presence of the cold surface ensures that most of the upper channel is almost uniformly cold and the local rate of heat transfer is almost zero. Thus almost all of the heat transfer arises in decreasingly-sized domain near the upstream corners as $\epsilon \to 1$, and therefore Nu reduces as $\epsilon \to 1$ for cases where $\kappa < 1$.

Returning to the Ra = 100 case shown in Fig. 5, we also see the behaviour of the 2-cell and 4-cell solutions. When Ra = 100 and there is no block present, the 1-cell and 2-cell modes have the respective critical values, $\mathrm{Ra}_c = 4\pi^2$ and $\mathrm{Ra}_c = 6.25\pi^2$, and therefore we would expect the latter flow to be weaker than the former when $\epsilon = 0$. As ϵ increases from zero, the 2-cell flow weakens quite quickly and eventually it collapses onto the 4-cell curve in what is effectively a supercritical pitchfork bifurcation in the direction of decreasing ϵ. The 1-cell flow does the same but at larger values of ϵ. It is interesting to note that lowest value of ϵ for which the 1-cell solution disappears is for large values of κ, while the first 2-cell solutions disappears when κ is small. We also note that, as $\epsilon \to 1$, the values of Nu for the 4-cell solutions tend towards the value of κ. We suspect that all the 1-cell branches will collapse onto a 4-cell branch as ϵ increases, but this may only be tested using a considerably finer grid than we have used here.

When Ra increases to 150 the shape of the solutions have essentially the same form. The points where the 1-cell and 2-cell branches join the 4-cell branch now take place at slightly larger values of ϵ because the increased buoyancy force associated with the larger Darcy-Rayleigh number means that the porous cavity has to be more restricted in order to herald a return to the 4-cell basic solution.

A significant change to this scenario when Ra = 200 is that the 2-cell branch appears to exhibit sudden jumps when κ is relatively small. These sections of the 2-cell branch still maintain the same form of left/right symmetry as was shown in Fig. 4, but some further cells appear, as shown in Fig. 7 where both frames correspond to the parameters $\kappa = 1/5$ and $\epsilon = 0.26$. The left hand frame corresponds to the left hand part of the appropriate solution branch in Fig. 5 and we have Nu = 3.364 and $\mathscr{C} = 4.849$. The right hand frame in Fig. 7 corresponds to the right hand part of the branch in Fig. 5 which joins the 4-cell branch; here Nu = 2.125 and $\mathscr{C} = 3.651$. This sudden jump only makes sense if the two parts of the solution curve are joined by an S-shaped segment, but this cannot be confirmed because the present numerical scheme can only solve for discrete values of ϵ. But it is worth pointing out that the appearance of the streamlines in the right hand frame of Fig. 7 shares the direction of flow at the corners of the block with the 4-cell conduction solution, and therefore it is a pattern which is an obvious (in an *a posteriori* sense) one to have which will eventually evolve into the 4-cell solution at larger values of ϵ.

A second change when Ra = 200 is that the 4-cell solution now exists when $\epsilon = 0$. The onset mode takes the form of $\theta \propto \cos 2\pi x \sin 2\pi z$, and the critical Darcy-Rayleigh number is $16\pi^2$; see (42). So while $\mathscr{C} \to 0$ as $\epsilon \to 0$ whenever $\mathrm{Ra} < 16\pi^2$, there is a nonzero limit when Ra takes larger values such as Ra = 200.

An alternative view is presented in Figs. 8 and 9 which single out the effect of having different values of Ra for a chosen set of values of κ. Attention is restricted here solely to 1-cell and 4-cell flows, as it is unlikely that 2-cell flows will form the dominant mode of convection in a unit cavity. Figure 8 shows the variation in Nu with ϵ for values of Ra from zero to 200 in increments of 25. While the lowest branch corresponds to Ra = 0 and is the no-flow solution, there is a segment of solution curve corresponding to Ra = 25 just above it when $\kappa = 1/100$, but which does not exist for the other selected values of κ. This (together with Fig. 10 below) suggests that the smallest possible critical value of Ra for the present system lies below 25, and corresponds to a highly insulated block with a value of ϵ which is likely to lie somewhere between 0.4 and 0.6. More precisely, we have computed the critical values of Ra_c as a function of ϵ and for $\kappa = 1/100$, $1/200$ and $1/400$. Table 2 shows the detailed data for $\kappa = 1/100$ which, when graphed, appears not to be noisy at all, and therefore we have confidence that the extrapolation process we used to determined the critical values works well.

Table 2: The variation of the critical value of Ra for the onset of convection as a function of ϵ when $\kappa = 0.01$. A 100×100 grid was used for these computations.

ϵ	Ra_c
0.40	23.3090
0.42	23.0233
0.44	22.7966
0.46	22.6227
0.48	22.4960
0.50	22.4138
0.52	22.3706
0.54	22.3611

ϵ	Ra_c
0.56	22.3815
0.58	22.4272
0.60	22.4954
0.62	22.5813
0.64	22.6823
0.66	22.7953
0.68	22.9180
0.70	23.0488

According to the data in Table 2 the smallest possible Ra_c when $\kappa = 1/100$ is $\mathrm{Ra} \simeq 27.360$ and this arises when $\epsilon \simeq 0.5382$. However, we investigated the possibility that Ra_c might take the form of a power series, $\mathrm{Ra}_c = \mathrm{Ra}_0 + \mathrm{Ra}_1\kappa + \mathrm{Ra}_2\kappa^2 + \cdots$ when κ is small. Table 3 shows how the critical value of Ra varies with n and κ.

Table 3: The variation of the critical value of Ra for the onset of convection as a function of ϵ for the given values of κ. A 100×100 grid was used for these computations.

ϵ	$\kappa = 1/100$	$\kappa = 1/200$	$\kappa = 1/400$
0.52	22.3706	22.2069	22.1208
0.54	22.3611	22.1892	22.1027
0.56	22.3815	22.2030	22.1127

Using the above series in κ for Ra_c, it is possible to show that the $\kappa \to 0$ limit is

$$\mathrm{Ra}_c \simeq 22.0152 \quad \text{when} \quad \epsilon \simeq 0.5423. \tag{43}$$

The lowest curve in each of the subframes in Fig. 8 corresponds to Ra = 0, the conduction profile. We see that, as ϵ increases the Nusselt number decreases when $\kappa < 1$ and increases when $\kappa > 1$ because of the increasing dominance of the conductivity of the block over that of the porous medium. Once the Darcy-Rayleigh number is large enough we generally find that Nu increases as ϵ increases from zero before decreasing once more, although at lower values of Ra the Nu curves tend to have a more complicated behaviour.

Once ϵ is sufficiently large, in most cases the Nu curve appears to collapse onto the Ra = 0 curve. This is only an appearance, because the curves corresponding to different values of Ra when $\kappa = 100$ are clearly distinct, and this is confirmed in Fig. 9 which displays the analogous $\mathscr{C}$ curves. The apparent merging of the Nu curves is an artefact of the presence only of relatively weak flow in the corners of the cavity. This is seen very clearly in Fig. 9. Thus the great majority of the upward heat transfer takes place by conduction, although for $\kappa = 100$ the corner region circulations remain quite strong, as seen in Fig. 9.

Finally, in Fig. 10 we show the classical variations of Nu and $\mathscr{C}$ with Ra. In all cases these correspond to the basic state 4-cell profile when Ra is sufficiently small, and a strongly convecting 1-cell profile once Ra exceeds the critical value which is dependent on both κ and ϵ. Thus, when ϵ takes small values, then the presence of the block, even for extreme values of κ such as $1/100$ and 100, has little effect of the onset criterion. But as ϵ increases this effect becomes much stronger in terms of the amount of variation there is as κ varies. In general Ra_c decreases as ϵ increases whenever κ is small, and the opposite arises when κ is large. Table 4 gives the onset values of Ra corresponding to the data shown in Fig. 10; we have also given data for $\kappa = 1/1000$ and $\kappa = 1000$, for comparison with the extreme values of $\kappa = 1/100$ and $\kappa = 100$ which have used in this paper.

From the graphs of Nu, we see that convective onset is confirmed to take place at values which are larger than about 25 in all cases, except for when κ is very small, as discussed earlier and depicted in Table 2. It is also clear that, when $\epsilon = 3/4$, and κ takes values at or above 5, then convective onset must arise when Ra > 200.

Table 4: Critical values of Ra of the given values of ϵ and κ. Using a 100×100 grid.

κ	$\mathrm{Ra}(\epsilon = 1/4)$	$\mathrm{Ra}(\epsilon = 1/2)$	$\mathrm{Ra}(\epsilon = 3/4)$
$1/1000$	27.7200	22.1546	22.8471
$1/100$	27.8813	22.4212	23.4070
$1/5$	31.6650	28.0744	34.8390
$1/3$	33.1602	30.7855	40.4023
$1/2$	35.6186	35.6493	50.9271
1	39.6424	45.6859	74.7541
2	43.8364	59.7685	115.675
3	46.0249	69.0566	150.167
5	48.3466	80.3586	>200
100	53.1571	110.352	>200
1000	53.4582	112.534	>200

5 Conclusions

In this paper we have sought to determine in as comprehensive a fashion as possible what the effect is of the presence of a centrally-placed square solid block on the onset and development of Darcy-Bénard convection in a square porous cavity. Apart from the usual Darcy-Rayleigh number, Ra, the two new governing parameters are the length and conductivity ratios, ϵ and κ.

We have found that the size of the block and its conductivity relative to that of the porous medium have a very strong effect on the basic state and on the onset criterion. Generally, when the block has a small conductivity, then (1-cell) convection arises at a value which is lower than the $\epsilon = 0$ classical value of $4\pi^2$, and the opposite happens when the block is highly conducting. In addition the range over which Ra_c varies, when κ increases from very small to very large, itself increases as the block gets larger. By means of careful computations, we have determined that the smallest possible value of Ra_c is 22.0152 when $\epsilon = 0.5432$ and κ is very small.

We have also found that, in much of (Ra, κ) parameter space, the Nusselt number rises at first as ϵ increases from zero before decreasing again, a feature which is counter-intuitive because it might naïvely be thought that an obstruction would hinder convection. In most cases 1-cell convection is eventually extinguished as $\epsilon \to 1$, although the present numerical resolution is insufficient to determine if this remains true for very small values of κ.

The present computations may be extended in a variety of ways. One possibility is to consider larger values of Ra, but this will entail the categorisation of further steady convection patterns and the early occurrence of unsteady convection (Riley and Winters 1991 computed a value of 390.7 for the square porous cavity). One may also consider rectangular cavities, non-square blocks and other locations for the block. In many of these cases certain symmetries which are present in our computations will be lost, and this will have a strong effect on the general conclusions we have presented. Yet another possibility might be to use a network of blocks each separated by a porous medium as a model for a bidisperse porous medium. Finally, we might also consider the effect of local thermal non-equilibrium. While this would introduce two further parameters it might nevertheless cause some qualitative changes in the solutions at moderate values of Ra. Banu and Rees (2002) showed that, when the interfacial heat transfer coefficient is large and porosity-modified conductivity ratio is small, then convection arises with a wavenumber which is large compared with π. The implication for the present configuration is that this might well cause many more convection cells to arise within the cavity.

Acknowledgements

The authors would like to thank the reviewers for their kind words and for their comments which served to improve the manuscript.

References

Acosta, R., Sen, M., Ramos, E.: Single-phase natural circulation in a tilted square loop. Wärme- und Stoffübertr. **21**, 269–275 (1987).

Banu, N., Rees, D.A.S.: The onset of Darcy-Bénard convection using a thermal nonequilibrium model. International Journal of Heat Mass Transfer **45**, 2221–2228 (2002).

Bararnia, H., Soleimani, S., Ganji, D.D.: Lattice Boltzmann simulation of natural convection around a horizontal elliptic cylinder inside a square enclosure. International Communications in Heat and Mass Transfer **38 (10)**, 1436–1442 (2011).

Bhave, P., Narasimhan, A., Rees, D.A.S.: Natural convection heat transfer enhancement using adiabatic block: optimal block size and Prandtl number effect. International Journal of Heat and Mass Transfer **49**, 3807–3818 (2006).

Ehrhard, P., Mueller, U.: Dynamical behavior of natural convection in a single-phase loop. J. Fluid Mech. **217**, 487–518 (1990).

Gorman, M., Widmann, P.J., Robbins, K.A.: Chaotic flow regimes in a convection loop. Phys. Rev. Lett. **52**, 2241–2214 (1984).

Gordon, M., Ramos, E., Sen, M.: A one-dimensional model for a thermosyphon with known wall temperature. Int. J. Heat Fluid Flow **8**, 177–181 (1987).

Greif, R., Zvirin, Y., Mertol, A.: Transient and stability behavior in a natural-convection loop. ASME J. Heat Transfer **101**, 684–688 (1979).

Hooman, K., Merrikh, AA (Merrikh, A.A.: Theoretical analysis of natural convection in an enclosure filled with disconnected conducting square solid blocks. Transport in Porous Media **85**, 641–651 (2010).

House, J.M., Beckermann, C., Smith, T.F.: Effect of a centered conducting body on natural convection heat transfer in an enclosure. Numerical Heat Transfer A **18**, 213–225 (1990).

Jamalud-Din, S.-D., Rees, D.A.S., Reddy, B.V.K., Narasimhan, A.: Prediction of natural convection flow using a network model and numerical simulations inside an enclosure with distributed solid blocks. Heat and Mass Transfer **46**, 333–343 (2010).

Jiang, Y.Y., Shoji, M.: Thermal convection in a porous toroidal thermosyphon. Int. J. Heat Mass Transfer **45**, 3459–3478 (2002).

Keller, J.B.: Periodic oscillations in a model of thermal convection. J. Fluid Mech. **26**, 599–606 (1966).

Lavine, A.S., Greif, R., Humphrey, J.A.C.: A 3-dimensional analysis of natural convection in a toroidal loop — the effect of Grashof number. Int. J. Heat Mass Transfer **30**, 251–262 (1987).

Lavine, A.S., Greif, R., Humphrey, J.A.C.: 3-dimensional analysis of natural convection in a toroidal loop — effect of tilt angle. ASME J. Heat Transfer **108**, 796–805 (1986).

Magomedbekov, Kh.G., Ramazanov, M.M.: Hydrothermal convection in a thin porous ring. Fluid Dyn. **29**, 740–744 (1994).

Magomedbekov, Kh.G., Ramazanov, M.M.: Linear analysis of convective instability of fluid in horizontal annular cavity filled with porous medium. Izv. Akad. Nauk. Mekh. Zhid. Gaza **3**, 19–26 (1996).

Malkovsky, V.I., Pek, A.A.: Conditions for the onset of thermal convection of a homogeneous fluid in a vertical fault. Petrology **5**, 381–387 (1997).

Mertol, A., Greif, R.: A review of natural circulation loops. In Natural Convection: Fundamental and Applications (Aung, W., Kakag, S., Viskanta, R. eds.), pp.1033–1071, Hemisphere, New York (1985)

Mertol, A., Greif, R., Zvirin, Y.: Two-dimensional study of heat-transfer and fluid-flow in a natural convection loop. ASME J. Heat Transfer **104**, 508–514 (1982).

Nield, D.A.: A note on convection in fracture loops. Transport in Porous Media **109**, 195–199 (2015).

Nield, D.A., Bejan, A.: Convection in Porous Media (4th edition), Springer, New York (2013).

Paterson, I., Schlanger, H.P.: Convection in a porous thermosyphon imbedded in a conducting medium. Int. J. Heat Mass Transfer **35**, 877–886 (1992).

Postelnicu, A., Scurtu, N.: Effect of asymmetry on the steady convection in a vertical torus filled with a porous medium. Strojniski Vestnik. J. Mech. Engng. **51**, 501–508 (2005).

Rahman, Md.M., Alim, M.A., Saha, S., Chowdhury, M.K.: Effect of the presence of a heat conducting horizontal square block on mixed convection inside a vented square cavity. Nonlinear Analysis: Modelling and Control **14 (4)**, 531–548 (2009).

Ramazanov, M.M.: Convection in a obliquely heated thin porous elliptic ring. Fluid Dyn. **35**, 910–917 (2000).

Ramos, E., Castrejon, A., Gordon, M.: Natural convection in a two-dimensional square loop. Int. J. Heat Mass Transfer **33**, 917–930 (1990).

Rees, D.A.S.: Microscopic modelling of the two-temperature model for conduction in heterogeneous media. Journal of Porous Media **13**, 125–143 (2010).

Rees, D.A.S.: Convection of a Bingham fluid in a porous medium. Chapter 17 in: Handbook of Porous Media, 3rd edition (K. Vafai, ed.) CRC Press (2015).

Ridouane, E.H., Danforth, C.M., Hitt, D.L.: A 2-D study of chaotic flow in a natural convection loop. Int. J. Heat Mass Transfer **53**, 76–84 (2010).

Ridouane, E.H., Hitt, D.L, Danforth, C.M.: A numerical analysis of 3-D flow regimes in a toroidal natural convection loop. Int. J. Heat Mass Transfer **54**, 5253–5261 (2011).

Riley, D.S., Winters, K.H.: Time-periodic convection in porous media: the evolution of Hopf bifurcations with aspect ratio. J. Fluid Mech. **223**, 477–474 (1991).

Robillard, L., Nguyen, T.H., Vasseur, P.: Free convection in a two-dimensional porous loop. ASME J. Heat Transfer **108**, 277–283 (1986).

Roslan, R., Saleh, H., Hashim, I.: Natural convection in a differentially heated square enclosure with a solid polygon. The Scientific World Journal. Volume 2014, Article ID **617492**, 11 pages.

Sano, O.: Steady thermal convection in an annular region between two horizontal concentric cylinders. J. Phys. Soc. Japan **55**, 4234–4240 (1986).

Sano, O.: Cellular structure in a natural convection loop and its chaotic behavior. I. Experiment. Fluid Dynamics Research **8**, 189–204 (1991a).

Sano, O.: Cellular structure in a natural convection loop and its chaotic behavior. II.Theory. Fluid Dynamics Research **8**, 205–220 (1991).

Scurtu, N.D., Postelnicu, A., Pop, I.: Free convection between two horizontal cylinders filled with a porous medium — a perturbation solution. Acta Mech. **151**, 115–125 (2001).

Simmons, C.T., Sharp, J.M., Jr., Nield, D.A.: Modes of free convection in fractured low-permeability media. Water Resources Research **44**, W04331 (2007).

Stern, C.H., Greif, R.: Measurements in a natural-convection loop. Wärme- und Stoffübertr. **21**, 277–282 (1987).

Stern, C.H., Greif, R., Humphrey, J.A.C.: An experimental study of natural convection in a toroidal loop. ASME J. Heat Transfer **110**, 877–884 (1988).

Welander, P.: On the oscillatory instability of a differentially heated fluid loop. J. Fluid Mech. **29**, 17–30 (1967).

Figures

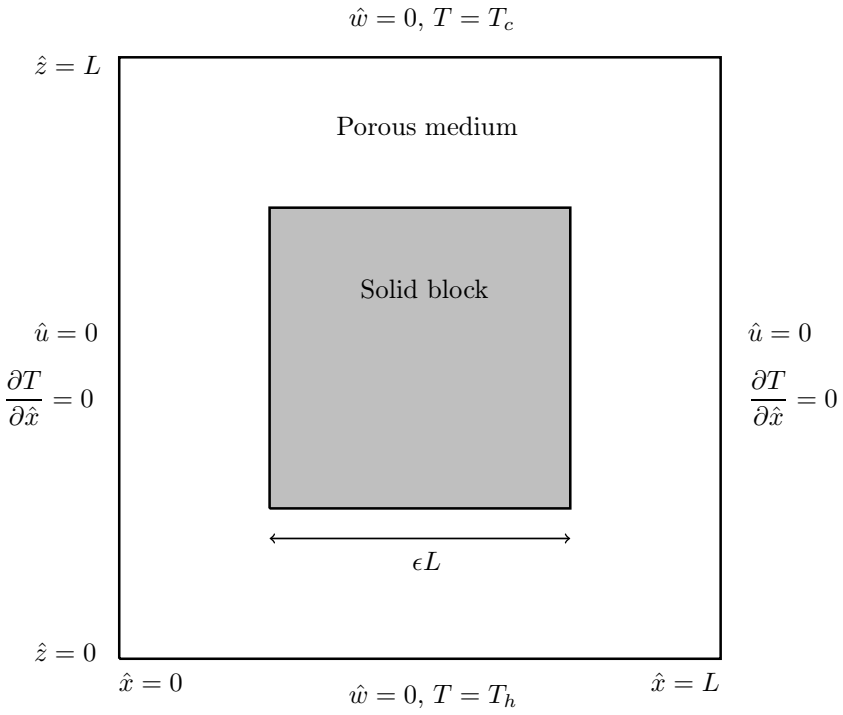

Figure 1: Definition sketch of the porous cavity with a centrally-placed solid conducting block embedded within it. Gravity acts vertically downwards.

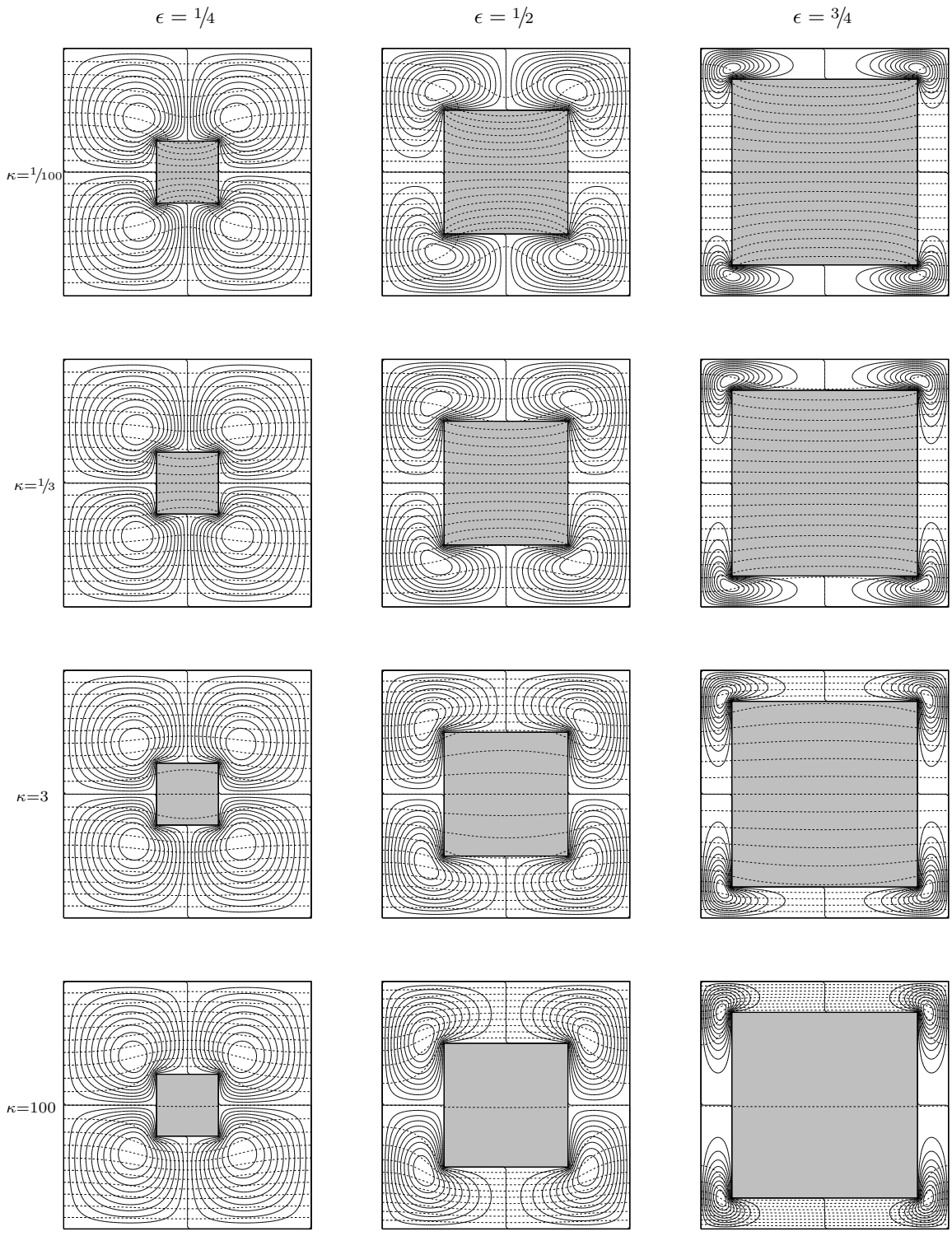

Figure 2. Showing the effect of the conductivity ratio, κ, and the size, ϵ, of the central solid block on the streamlines (continuous) and the isotherms (dashed) when Ra = 1, i.e. when nearly fully conducting conditions prevail. Streamlines and isotherms are drawn using 20 equal intervals between their respective maxima and minima; these conventions will be used in the rest of the paper.

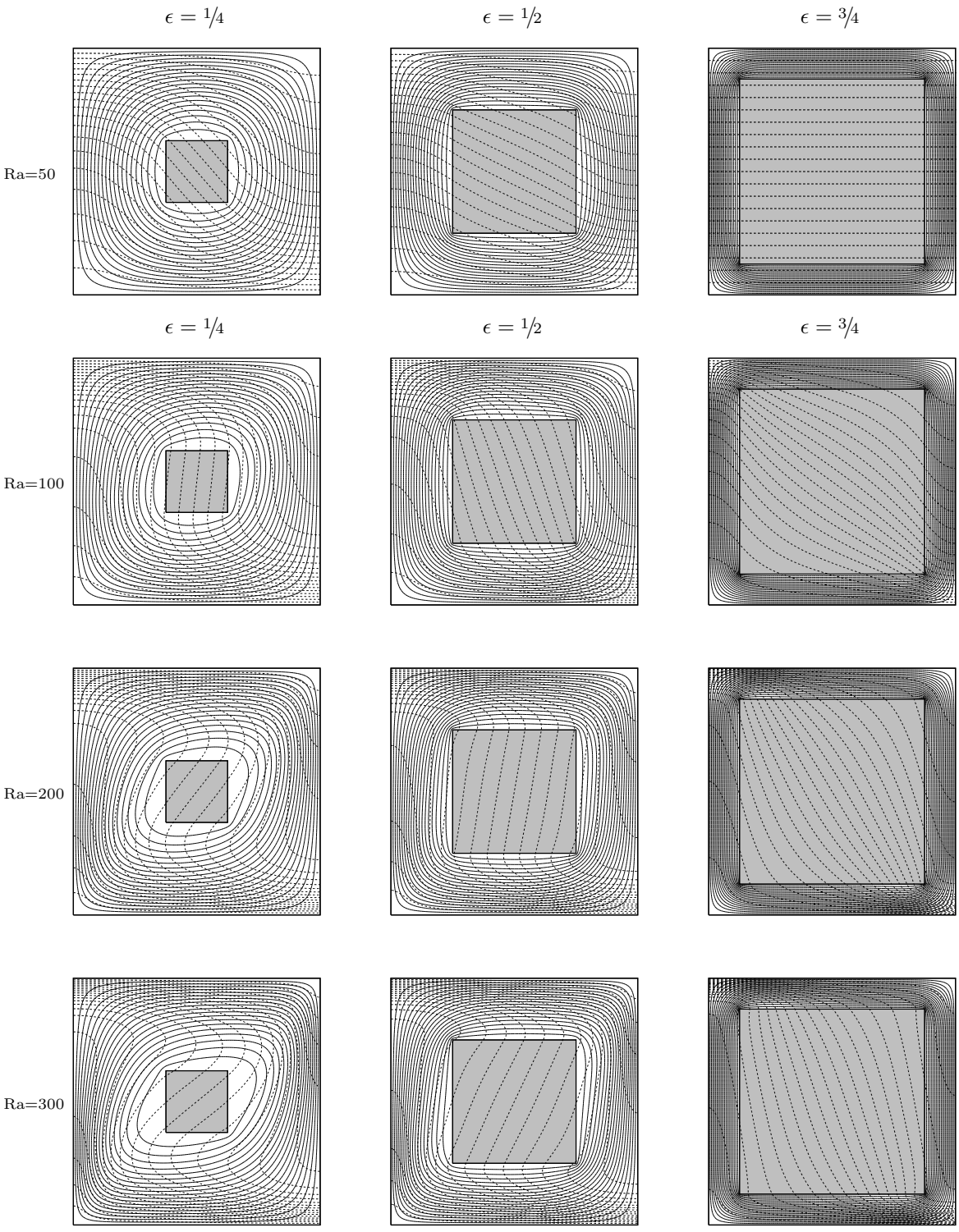

Figure 3. Showing the effect of the value of the Darcy-Rayleigh number and the size of the central solid block on the streamlines and isotherms when $\kappa = 1$, i.e. when the block and the porous medium have the same conductivity.

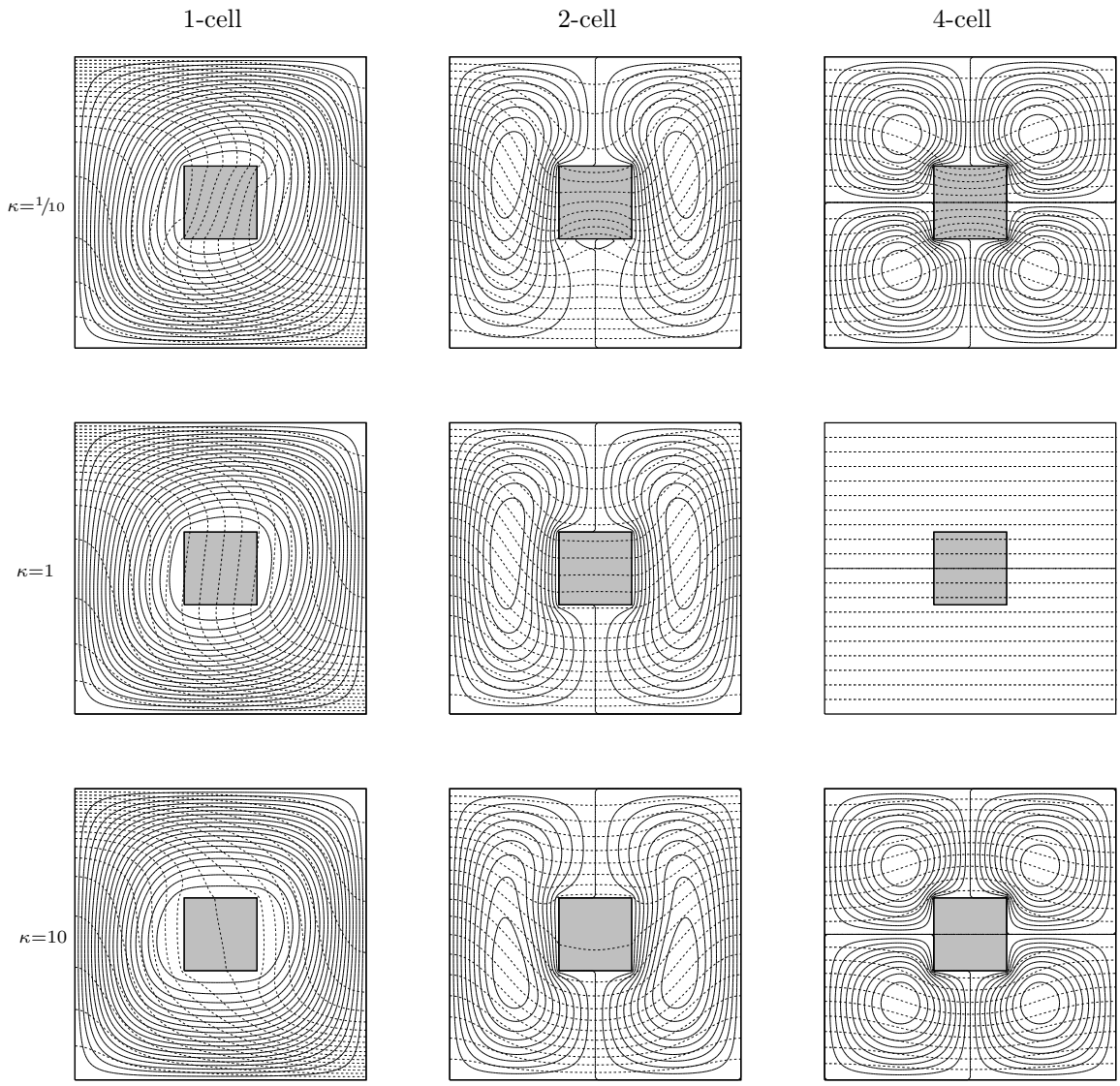

Figure 4. Showing the effect of the conductivity ratio, κ, on the flow patterns for the 1-cell, 2-cell and 4-cell cases. We have used the values, Ra = 100 and $\epsilon = 1/4$.

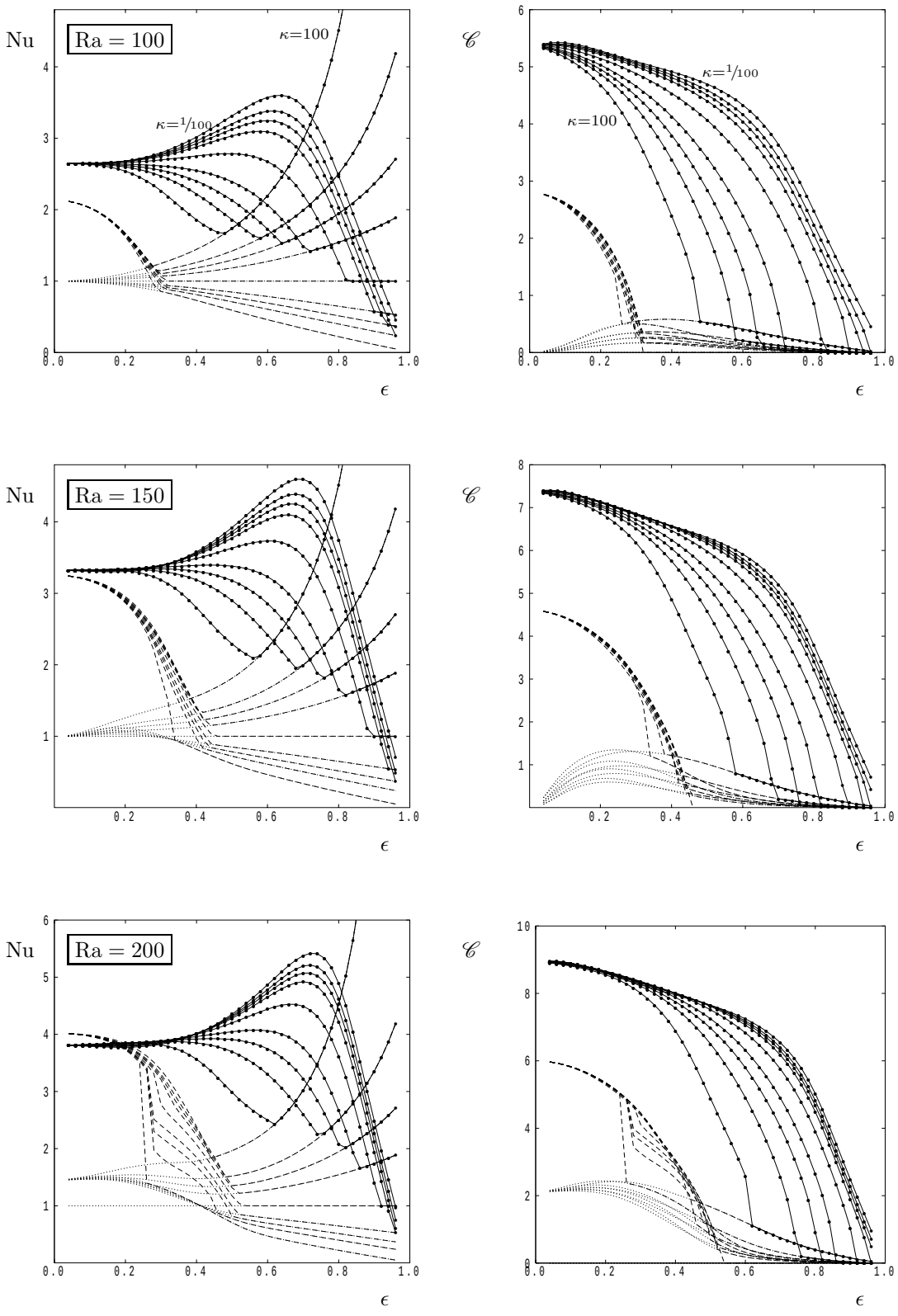

Figure 5: Variation in Nu and $\mathscr{E}$ with ϵ for Ra = 100, 150 and 200, and for the following values of κ: 1/100, 1/5, 1/3, 1/2, 1, 2, 3, 5 and 100. Continuous lines depict 1-cell flows, dashed lines 2-cell flows and dotted lines 4-cell flows. Solutions were obtained on a 100×100 grid and the bullets indicate admissible values of ϵ on this grid.

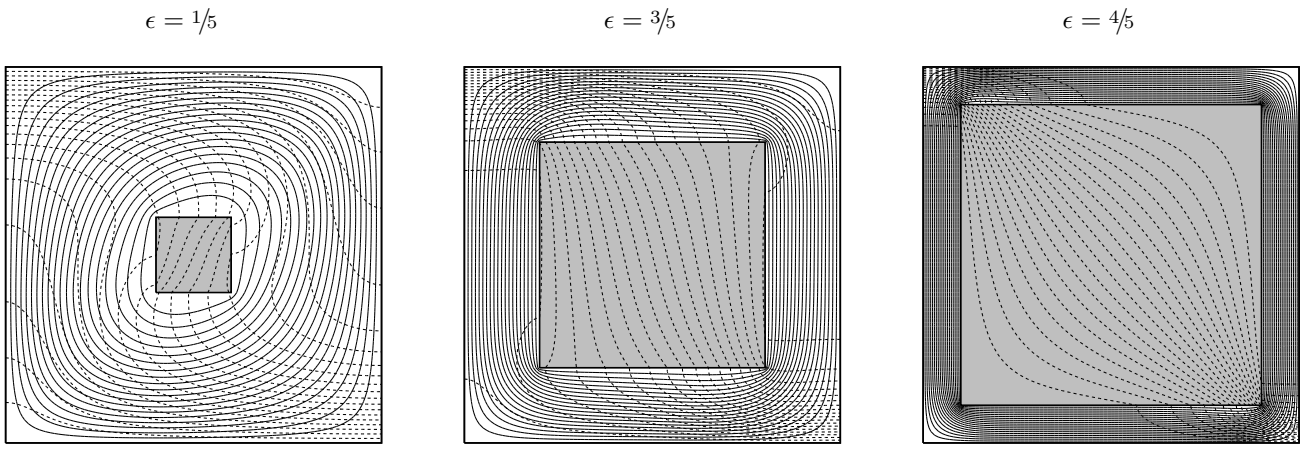

Figure 6. Showing the the streamlines and isotherms for Ra = 100 and $\kappa = 0.01$, for the given block sizes.

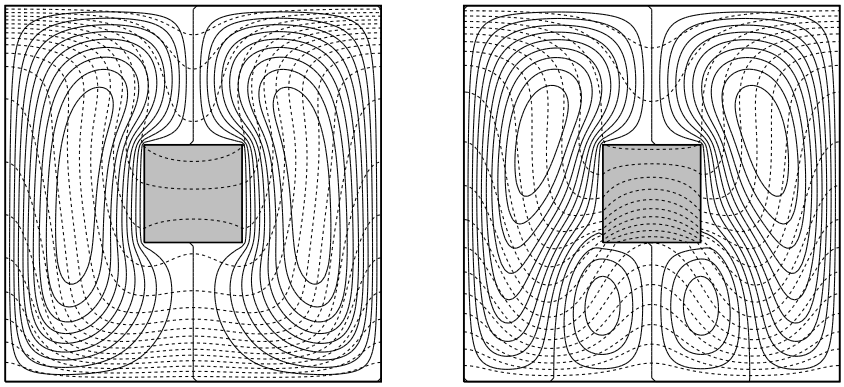

Figure 7. Showing the the streamlines and isotherms for two different 2-cell solutions for Ra = 100, $\kappa = 1/5$ and $\epsilon = 0.26$.

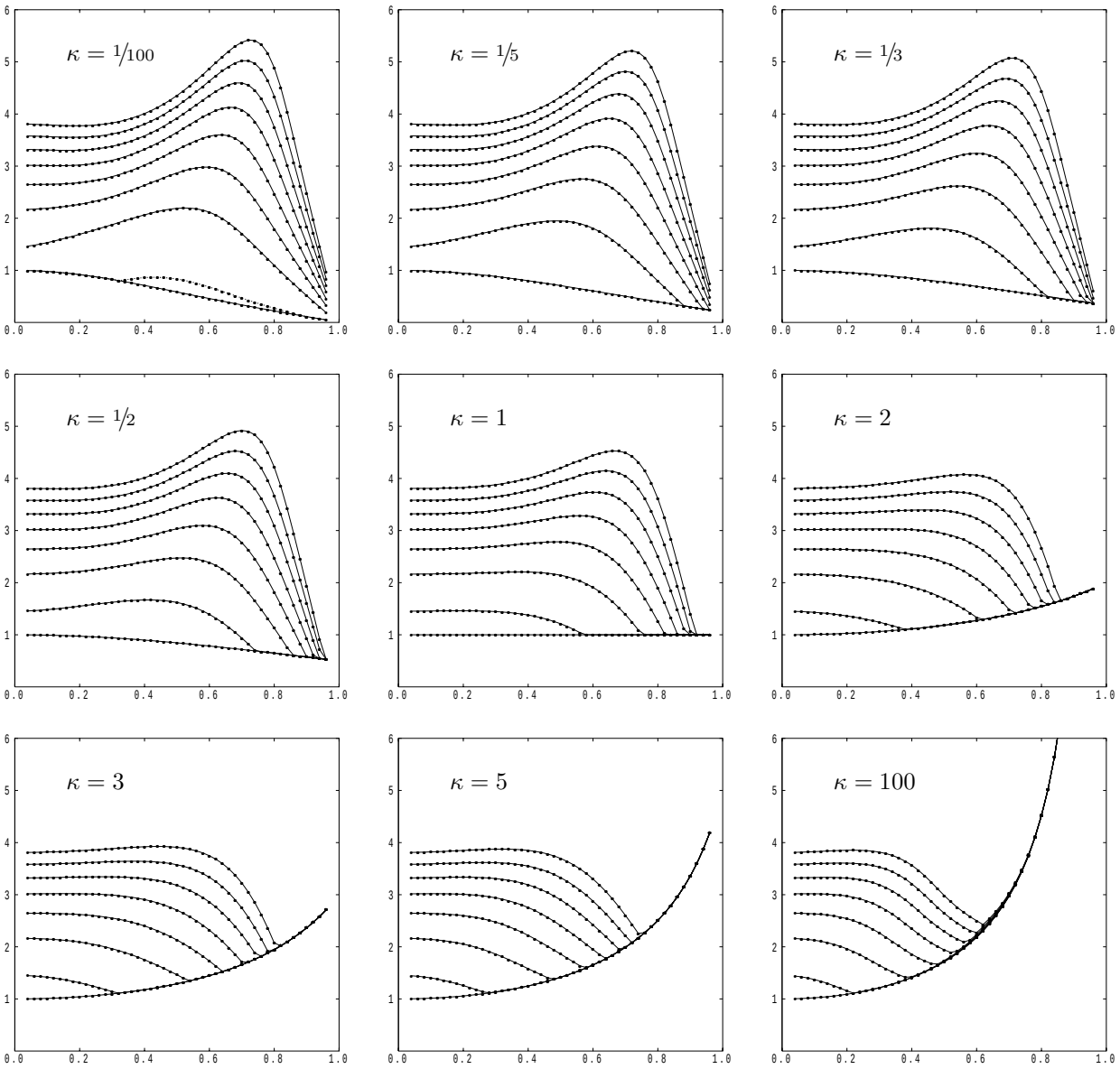

Figure 8. Variation of Nu with ϵ for Ra = 0, 25, 50, 75, 100, 125, 150, 175 and 200 (uppermost curve). Different frames correspond to the given values of κ. Solutions were obtained on a 100×100 grid.

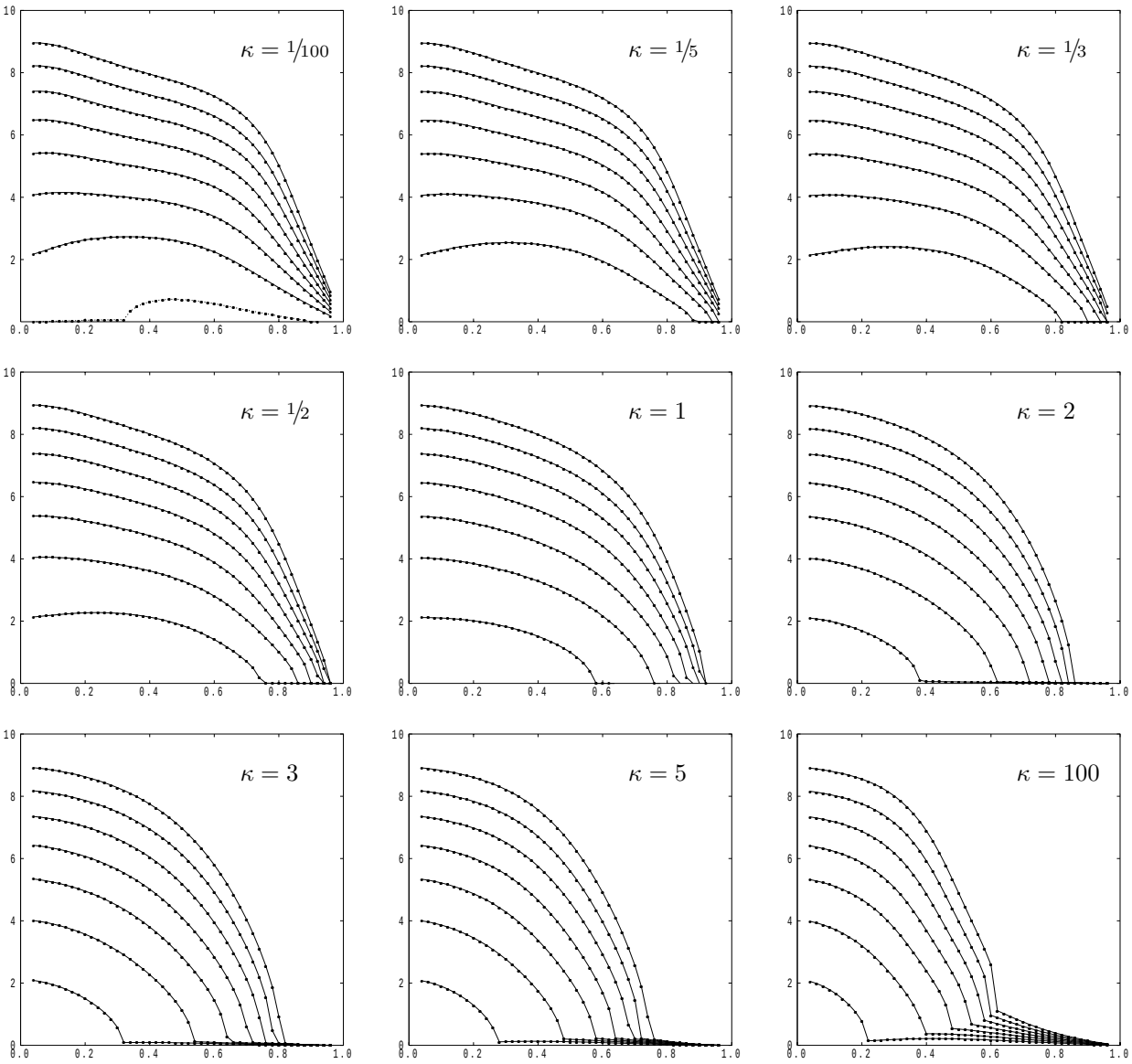

Figure 9. Variation of $\mathscr{C}$ with ϵ for Ra = 25, 50 75, 100, 125, 150, 175 and 200 (uppermost curve). Different frames correspond to the given values of κ. Solutions were obtained on a 100×100 grid.

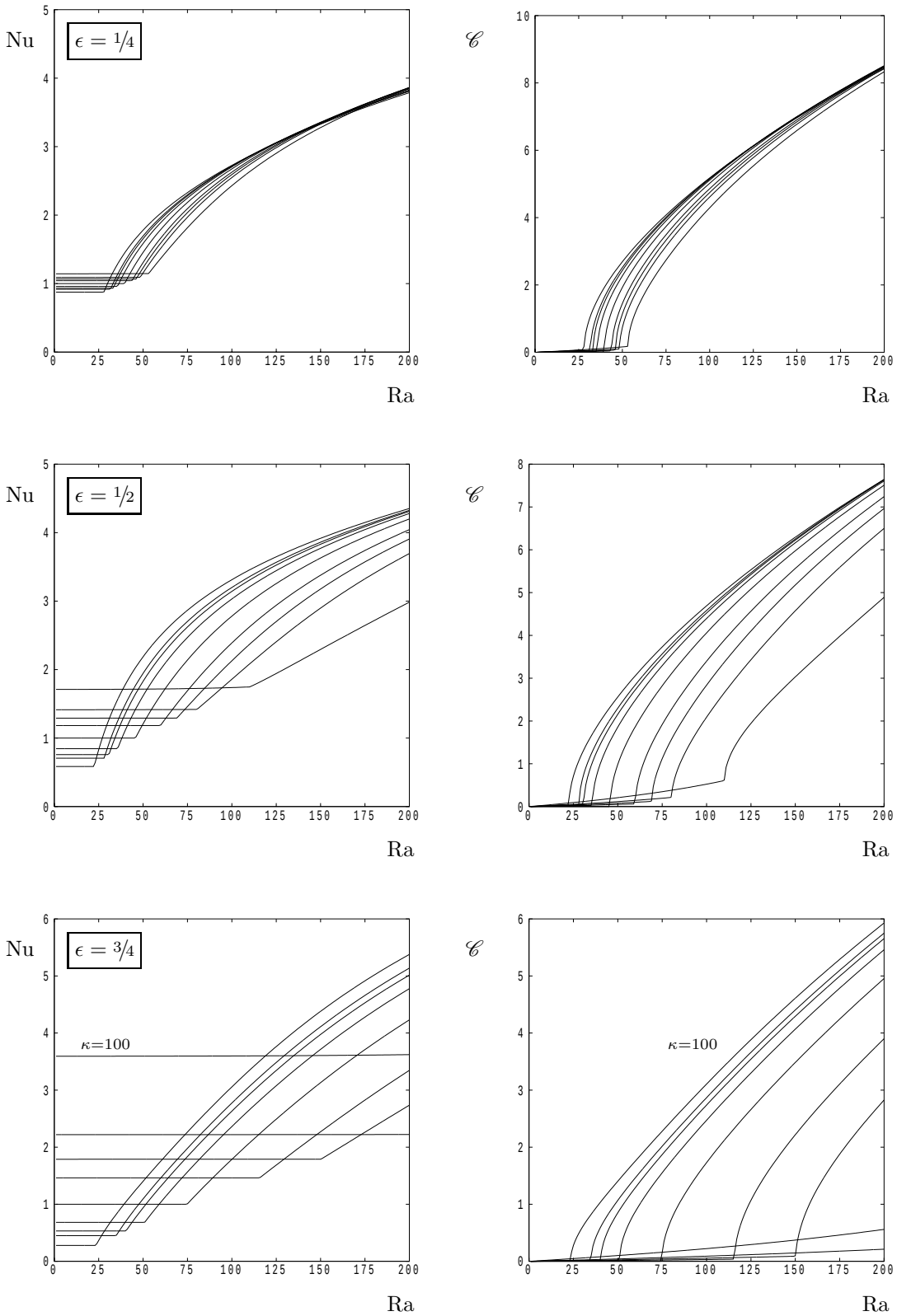

Figure 10. Variation of Nu and $\mathscr{C}$ with Ra for $\epsilon = 1/4$, $1/2$ and $3/4$, and for the following values of κ: $1/100$, $1/5$, $1/3$, $1/2$, 1, 2, 3, 5 and 100. Solutions were obtained on a 100×100 grid and the bullets indicate admissible values of ϵ on this grid. When Ra is small, the uppermost curve corresponds to $\kappa = 100$ and the lowest to $\kappa = 1/100$.